


**Atom-orbital qubit under nonadiabatic holonomic quantum control**Hongmian Shui<sup>1</sup>, Shengjie Jin<sup>1</sup>, Zhihan Li<sup>1</sup>, Fansu Wei<sup>1</sup>, Xuzong Chen<sup>1</sup>, Xiaopeng Li<sup>2,3,\*</sup> and Xiaoji Zhou<sup>1,4,†</sup><sup>1</sup>State Key Laboratory of Advanced Optical Communication System and Network, Department of Electronics, Peking University, Beijing 100871, China<sup>2</sup>State Key Laboratory of Surface Physics, Institute of Nanoelectronics and Quantum Computing, and Department of Physics, Fudan University, Shanghai 200438, China<sup>3</sup>Shanghai Qi Zhi Institute, Shanghai 200030, China<sup>4</sup>Collaborative Innovation Center of Extreme Optics, Shanxi University, Taiyuan, Shanxi 030006, China (Received 14 May 2021; revised 27 August 2021; accepted 17 November 2021; published 7 December 2021)

Quantum computing has been attracting tremendous efforts in recent years. One prominent application is to perform programmable quantum simulations of electron correlations in large molecules and solid-state materials, where orbital degrees of freedom are crucial to quantitatively model electronic properties. Electron orbitals unlike quantum spins obey crystal symmetries, making the atomic orbital in optical lattices a natural candidate to emulate electron orbitals. Here, we construct an atom-orbital qubit by manipulating  $s$  and  $d$  orbitals of atomic Bose-Einstein condensation in an optical lattice. Noise-resilient single-qubit gates are achieved by performing holonomic quantum control, which allows geometrical protection. We find it is critical to eliminate the orbital leakage error in the system. Our work opens up wide opportunities for atom-orbital-based quantum information processing, of vital importance to programmable quantum simulations of multiorbital physics in molecules and quantum materials.

DOI: [10.1103/PhysRevA.104.L060601](https://doi.org/10.1103/PhysRevA.104.L060601)

Orbital degrees of freedom are essential to the quantitative description of electrons in large molecules [1] and solid-state materials [2]. The complex interplay of spin, charge, and orbital is key to the emergence of novel electron phenomena such as multiferroics [2], unconventional superconductivity [3], and exotic molecular spin filtering [4,5]. Incorporating orbitals lies at the heart of accurate quantum chemistry calculations [1] and adds substantial computation complexity in simulating many-body electron correlation. With quantum computing, the overall computation complexity of quantum algorithms for quantum chemistry calculation has been reduced to polynomials [6,7], which has triggered much recent research effort on experimental demonstration of such quantum algorithms with superconducting qubits [8,9] and trapped ions [10,11]. However, using these qubits to emulate electron orbitals meets the experimental challenge of expensive qubit encoding [8] and demanding Hamiltonian engineering to impose precise orbital symmetry [12], and consequently the captured multiorbital effect in the experiments is rather limited [8,9].

With ultracold atoms confined in optical lattices, the atom-orbital wave function obeys the same crystalline symmetry as the electron orbitals [13], making the atom-orbital qubit an ideal qubit candidate to perform programmable quantum simulations of electron orbitals in molecules and solid materials. There has been fascinating progress made in controlling atom orbitals in optical lattices for quantum simulations of exotic

superfluids [14–19] and topological quantum states [20–23]. However, their gate-based universal quantum control is still lacking, leaving orbital qubit quantum computing so far unachieved.

In this Letter, we construct an atom-orbital qubit using  $s$  and  $d$  orbitals of a one-dimensional optical lattice. We have measured the orbital relaxation time ( $T_{\text{relax}}$ ) and the dephasing time ( $T_2$ ), finding  $T_{\text{relax}} = 4.5 \pm 0.1$  ms and  $T_2 = 2.1 \pm 0.1$  ms in our experiment. By programming lattice modulation, we reach universal nonadiabatic holonomic quantum gate control [24,25] over the atom-orbital qubit, which exhibits noise resilience against laser fluctuations due to geometrical protection. We demonstrate the holonomic quantum control of Hadamard and  $\pi/8$  gates, which form a universal gate-set for single-qubit rotation. The lattice modulation pulses are programmed to minimize orbital leakage error, which is the key to reach high-fidelity holonomic quantum control of atom-orbital qubits. We implement quantum process tomography (QPT) on the orbital qubit to measure the full density matrix, from which the obtained average gate fidelity is 98.36(10)%.

*Atom-orbital qubit.* Our experiment is based on a <sup>87</sup>Rb Bose-Einstein condensate (BEC) with  $2 \times 10^5$  atoms confined in a one-dimensional optical lattice. The lattice potential takes the form of  $V_p(x) = V_0 \cos^2(2\pi x/l)$ , with  $V_0$  being the lattice depth and  $l$  the wavelength of the laser forming the lattice, which is 1064 nm in this experiment. The lattice depth  $V_0$  is five times the laser recoil energy ( $E_r = \hbar^2/2ml^2$ ), with  $m$  being the atomic mass. With lattice confinement, atoms acquire orbital degrees of freedom, as each lattice site contains localized Wannier orbitals— $s$ ,  $p$ ,  $d$ , ...[13], whose quantum superposition gives multiple Bloch bands. Having atoms

\*xiaopeng\_li@fudan.edu.cn

†xjzhou@pku.edu.cn

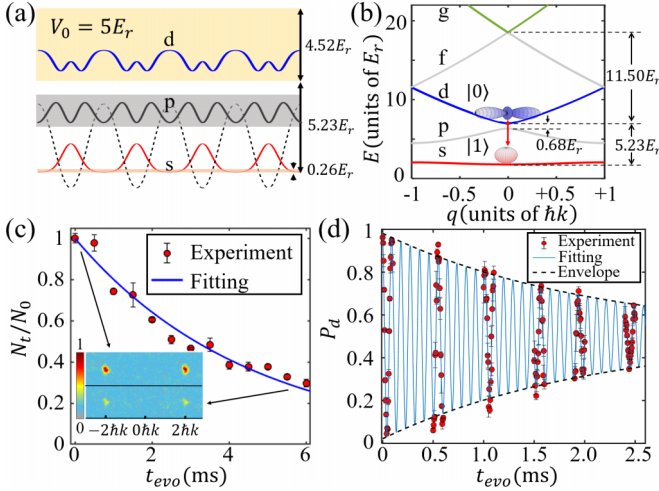


FIG. 1. Atom-orbital qubit in a one-dimensional optical lattice. (a) The Bloch wave-function amplitude of the  $s$ ,  $p$ , and  $d$  bands at zero quasimomentum. The  $s$  and  $d$  states constitute our orbital qubit. The dashed line represents the optical lattice potential. (b) The band-gap structures in our experimental optical lattice. The energy bands from bottom to top are  $s$ ,  $p$ ,  $d$ ,  $f$ , and  $g$  bands, respectively. (c) Measurement of relaxation time  $T_{\text{relax}}$  in the decay dynamics of the  $d$ -band population. The red dots correspond to the time evolution of the atom number  $N_d$  in the  $d$  band by time-of-flight measurement. The blue line represents fitting to the function  $N_d(t) = N_0 \exp(-t/T_{\text{relax}})$ . The relaxation time is determined as  $T_{\text{relax}} = 4.5$  ms. (d) Measurement of dephasing time  $T_2$  through Ramsey interference. The red dots show the measured time evolution of the proportion of atoms  $P_d$  in the  $d$ -band by the band-mapping method. The blue line represents the fitting function  $P_d = A \exp(-t/T_2) \sin(\omega t + \phi) + B$ , with the black line being the envelope of the Ramsey oscillations. We have a dephasing time of  $T_2 = 2.1$  ms by fitting.

condense at lattice quasimomentum  $k = 0$ , the orbital quantum state is described by the density matrix

$$\rho = \sum_{\nu\nu'} \rho_{\nu\nu'} |\nu\rangle \langle \nu'|, \quad (1)$$

where  $|\nu = s, p, d, \dots\rangle$  represents the Bloch mode at  $k = 0$  of the  $\nu$ -orbital band. In order to control the orbital state, we apply lattice modulation with a particular frequency  $\omega$  to resonantly couple  $s$  and  $d$  orbitals (see Fig. 1), which introduces an additional potential,

$$\Delta V(x, t) = A \sin(\omega t + \varphi) V_p(x), \quad (2)$$

with both amplitude  $A$  and phase  $\varphi$  programmable in our experiment (see Supplemental Material [26]). With leakage to other orbitals neglected, the system corresponds to a two-level system, defining our atom-orbital qubit, with  $|d\rangle$  and  $|s\rangle$  being orbital states identified as the qubit basis states  $|0\rangle$  and  $|1\rangle$ . In our experimental lattice setup, the energy gap between  $s$  and  $d$  bands has a large detuning from the energy gap between other orbitals except the gap from the  $s$  band to the  $p$  band. Despite the absence of the energy suppression of the  $s$  to  $p$  transition, this transition is forbidden due to the inversion symmetry present during the lattice modulation. The transitions from the  $s$  orbital to the undesired orbitals are thus avoided, either by energy suppression or by symmetry.

For qubit initialization, we selectively load the atomic BEC into the lattice using our previously developed shortcut preparation method [27], with which we are able to initialize the qubit to an arbitrary state,  $|\psi\rangle = \cos\theta|0\rangle + \sin\theta e^{i\phi}|1\rangle$ , within  $250 \mu\text{s}$ . For qubit readout, we implement a time-of-flight quantum state tomography (TOFQST), which extracts the full information of the density matrix  $\rho_{\nu\nu'}$  from the atomic momentum distribution (see Supplemental Material [26]). In the experiment, we prepare a set of six complementary initial states,  $\mathfrak{S} \equiv \{|0\rangle, |1\rangle, |+\rangle, |-\rangle, |+i\rangle, |-i\rangle\}$ , whose measured state fidelities are 99.96(2)%, 99.88(5)%, 99.30(11), 99.37(10)%, 99.83(5)%, and 99.98(1)%. The averaged fidelity is 99.72(7)%.

By initializing to the excited  $d$ -orbital state, namely,  $|0\rangle$ , we measure the time ( $t$ ) evolution of the atom number  $N_d$  in the  $d$  band and obtain  $N_d(t)$ . Fitting this function to  $e^{-t/T_{\text{relax}}}$ , we extract the relaxation time  $T_{\text{relax}}$ , which is  $4.5 \pm 0.1$  ms [Fig. 1(c)]. To measure the dephasing time  $T_2$ , we prepare the orbital superposition state  $[|0\rangle + |1\rangle]/\sqrt{2}$ . For the energy splitting between  $s$  and  $d$  orbital bands in the lattice, this superposition state develops Ramsey interference fringes in dynamics. The time dependence of the off-diagonal term has the form [Fig. 1(d)]

$$\text{Re}[\rho_{sd}(t)] \sim e^{-t/T_2} \cos(\Omega t + \phi), \quad (3)$$

with  $\Omega$ ,  $\phi$ , and  $T_2$  determined by fitting the experimental data gotten by the band-mapping method. We obtain a  $T_2$  time of  $2.1 \pm 0.1$  ms.

*Nonadiabatic holonomic orbital gate construction.* With the optical potential in Eq. (2), we have a qubit control Hamiltonian  $H(t)$  of the form

$$\frac{1}{2} \Delta \sigma_z + \frac{1}{2} \lambda [-\cos(\omega t + \varphi) \sigma_y + \sin(\omega t + \varphi) \sigma_x], \quad (4)$$

where  $\Delta$  is the gap between the  $s$  and  $d$  bands at quasimomentum  $k = 0$  ( $\Delta = 5.23E_r$  in our experiment), and the induced coupling by the lattice modulation is

$$\lambda = A \int dx V_p(x) \phi_d(x) \phi_s(x), \quad (5)$$

with  $\phi_{\nu=s,d}(x)$  being the Bloch function of the  $\nu$ -orbital band at  $k = 0$ . With the resonant coupling  $\omega \approx \Delta$ , the overall quantum gate operation time is determined by  $1/\lambda$ . To avoid nonresonant transitions to other bands, predominately the  $g$  band, which has an energy gap from the  $s$  band,  $\Delta_{sg} (= 16.73E_r \gg \Delta)$ , it is required that  $\lambda \ll |\Delta_{sg} - \omega|$ , which sets an upper limit for the amplitude of lattice modulation. For this requirement, it becomes more desirable to construct nonadiabatic quantum gates, as the adiabatic control would be too slow—the total adiabatic evolution time is required to be much longer than  $1/\lambda$  to maintain quantum adiabaticity.

We implement nonadiabatic holonomic orbital control based on a dynamical invariant of the Hamiltonian in Eq. (4),  $I = (\Delta - \omega) \sigma_z + \lambda [-\cos(\omega t + \varphi) \sigma_y + \sin(\omega t + \varphi) \sigma_x]$  [24,25], with its instantaneous eigenstates  $|\psi_{\pm}(t)\rangle$ . Through one period ( $T = 2\pi/\omega$ ) of quantum evolution, an initial quantum state  $\sum_n c_n |\psi_n\rangle$  is transformed to

$\sum_n c_n e^{i(\gamma_n^g + \gamma_n^d)} |\psi_n\rangle$ , with the accumulated geometrical phase  $\gamma_n^g = \int_0^T dt \langle \psi_n(t) | i \partial_t | \psi_n(t) \rangle$  and the dynamical phase  $\gamma_n^d = -\int_0^T dt \langle \psi_n(t) | H(t) | \psi_n(t) \rangle$ . The wave-function evolution in the dynamical invariant eigenbasis during the holonomic quantum control resembles quantum adiabatic dynamics [24,25]. The geometrical phase only depends on the solid angle enclosed by the evolution path of  $|\psi_n(t)\rangle$  on the Bloch sphere [28]. The holonomic gate is thus a generalization of the adiabatic geometrical gate [29]. This gate has intrinsic resilience against experimental control errors for geometrical protection [30,31], which has been demonstrated with liquid NMR [32,33], solid state [34–39], neutral atoms [40–42], ions [43–47], and superconducting qubits [48–53]. To exploit the geometrical protection, the dynamical phase has to be canceled, which corresponds to

$$\lambda^2 + \Delta(\Delta - \omega) = 0. \quad (6)$$

This gives the holonomic gate condition [25], which is explicitly satisfied in our lattice modulation design. The SU(2) rotation through one period of lattice modulation is then  $U_{\beta\varphi}(T) = \sum_{\pm} e^{i\gamma_{\pm}^g} |\psi_{\pm}(0)\rangle \langle \psi_{\pm}(0)|$ . This single-qubit rotation can be rewritten as

$$U_{\beta\varphi} = -e^{i\pi \sin \beta [-\sin \varphi \cos \beta \sigma_x + \cos \varphi \cos \beta \sigma_y + \sin \beta \sigma_z]}, \quad (7)$$

with  $\beta$  being determined by the lattice modulation frequency— $\cos^2 \beta = \Delta/\omega$  ( $\beta \in [0, \pi/2]$ )—and the angle  $\varphi$  being controllable by programming the potential [Eq. (2)]. An arbitrary target of holonomic SU(2) rotation,  $U_{\text{target}}$ , is approached by combining multiple periods ( $M$  times) of lattice modulation, which gives a concatenated unitary  $U = U_{\beta_M \varphi_M} U_{\beta_{M-1} \varphi_{M-1}} \dots U_{\beta_2 \varphi_2} U_{\beta_1 \varphi_1}$ . The parameter sequence  $(\beta_j, \varphi_j)$  is determined by optimizing the gate fidelity  $F = |\text{tr}(U^\dagger U_{\text{target}})|/2$ . We then obtain a control sequence of lattice modulation frequency, amplitude, and phase, denoted by  $\Theta_j \equiv (\omega_j, A_j, \varphi_j)$ . With this scheme, we expect gate fidelities above 99.999% using  $M \leq 5$  for  $X, Y, Z$ , Hadamard, and  $\pi/8$  gates under the idealized model in Eq. (4).

However, in comparing the results of the ideal model with a more precise multiorbital numerical simulation that incorporates all continuous degrees of freedom of the lattice (see Supplemental Material [26]), we find significant discrepancy. Figure 2 illustrates one example of state evolution under a constructed holonomic  $X$  gate. In the example shown in Fig. 2(a), the gate fidelity obtained by the multiorbital numerical simulation is below 85%. The sizable difference from the ideal model is attributed to the leakage to other unwanted orbitals. Even a small fraction of the  $g$ -band population below 5% is found to strongly disturb the qubit evolution on the Bloch sphere [Fig. 2(a)]. To resolve the problem of orbital leakage, we develop an orbital leakage elimination protocol (see Supplemental Material [26]), where the leakage error is minimized by optimizing the control sequence  $\Theta_j$ . With the optimal control sequence designed for the holonomic  $X, Y, Z$ , Hadamard, and  $\pi/8$  gates (see Supplemental Material [26]), the gate fidelity is improved to above 98% in the multiorbital numerical simulation. The orbital leakage elimination protocol is implemented in our experiment for high-fidelity realization of holonomic gates.

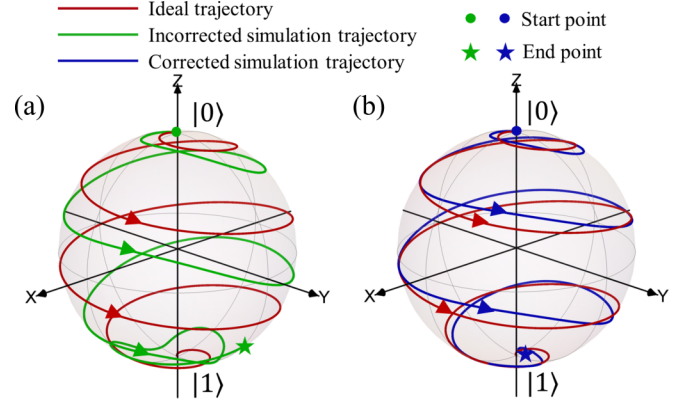


FIG. 2. Simulated time evolution of the  $|0\rangle$  state on the Bloch sphere under the holonomic  $X$  gate. North and south poles of Bloch sphere denote the  $|d\rangle$  and  $|s\rangle$  orbital states. The red curve shows the ideal state trajectory under the holonomic control according to the idealized qubit model [Eq. (4)]. The blue (green) curve shows the state trajectory by the multiorbital numerical simulation, with (without) the orbital leakage error eliminated.

*Holonomic quantum orbital gate fidelities.* In the experiment, we implement holonomic orbital gates taking the control sequences as designed with our orbital leakage elimination protocol. The band population dynamics during the gate operation has a very good agreement with our multiorbital numerical simulation (See Supplemental Material, Fig. S5 [26]). Figure 3 shows the experimental realization of the holonomic  $X$  gate. The atomic BEC is initialized in the quantum state  $| -i \rangle$ . We then perform the holo-

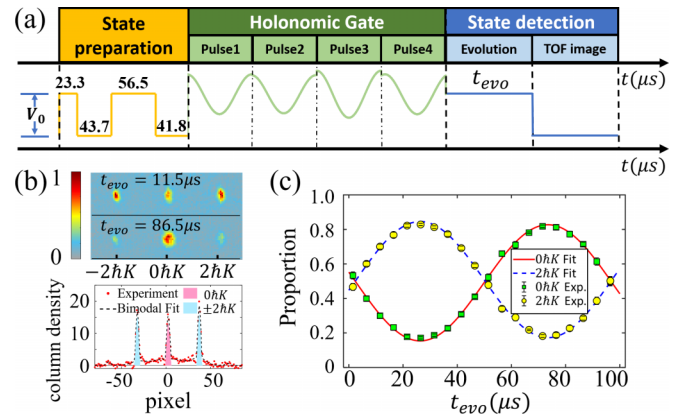


FIG. 3. Experimental realization of the holonomic quantum gates. (a) Experimental procedures of performing the holonomic  $X$  gate on the initial state,  $| -i \rangle$ . The numbers on top of the square pulses in panel (a) represent the time durations in units of microseconds. (b) Time-of-flight patterns at different evolution times. The condensed numbers of atoms at moments  $0\hbar K$  and  $\pm 2\hbar K$  are extracted following standard analysis in cold-atom experiments. (c) Oscillation dynamics of the atom number proportion at  $0\hbar K$  and  $\pm 2\hbar K$ . We average over four experimental runs for each data point, with the error bar denoting the standard statistical error. Here we set the lattice confinement  $V_0 = 5E_r$ .

TABLE I. Measured fidelities of the experimental holonomic quantum gates by TOFQST.

Initial state	$ 0\rangle$	$ 1\rangle$	$ +\rangle$	$ -\rangle$	$ +i\rangle$	$ -i\rangle$	Average
$X$ gate	99.92(3)	99.08(8)	98.87(11)	93.28(34)	98.75(9)	99.13(7)	98.17(16)
$Y$ gate	99.19(13)	99.71(6)	98.29(13)	96.91(20)	98.73(11)	99.15(8)	98.66(13)
$Z$ gate	97.87(14)	99.97(3)	97.47(18)	94.83(29)	99.14(11)	97.75(16)	97.84(17)
Hadamard	98.24(18)	98.38(11)	99.45(7)	97.90(20)	99.08(8)	96.77(23)	98.30(16)
$\pi/8$ gate	99.21(21)	99.76(7)	97.78(30)	95.94(41)	99.69(8)	99.28(24)	98.61(25)

nomical  $X$  gate control. The occupation of momentum  $\tilde{p} = 0$  and  $\tilde{p} = 2\hbar K$  (with  $K = 2\pi/l$ ) states are measured through time-of-flight (TOF), by which the full orbital qubit state is mapped out through TOFQST (see Supplemental Material [26]). This experimental procedure is repeated for all the initial states in  $\mathbb{S}$ . The fidelity ( $F$ ) averaged over the final states is 98.17(16)% (Table I), as calculated from the overlap of the density matrix measured in the experiment ( $\rho_{\text{exp}}$ ) with the theoretical construction ( $\rho_{\text{th}}$ ), i.e.,  $F = |\text{Tr}(\rho_{\text{exp}}\rho_{\text{th}}^\dagger)|/\sqrt{\text{Tr}(\rho_{\text{exp}}\rho_{\text{exp}}^\dagger)\text{Tr}(\rho_{\text{th}}\rho_{\text{th}}^\dagger)}$ . We also implement the holonomic  $Y$ ,  $Z$ , Hadamard, and  $\pi/8$  gates in the experiment, whose averaged final state fidelities are 98.66(13)%, 97.84(17)%, 98.30(16)%, and 98.61(25)%.

One way to construct a universal holonomic gate for single-qubit rotation is to combine Hadamard and  $\pi/8$  gates [54]. The other is to search for the control sequence numerically, whose universality is confirmed through our multiorbital numerical simulation. We randomly sample 100 Haar random  $\text{SU}(2)$  rotations and find all can be constructed by the concatenated unitary sequence with  $M \leq 5$ , producing final-state fidelities all above 98% (See Supplemental Material, Fig. S2 [26]).

To characterize the holonomic quantum gates directly, we further perform quantum process tomography (QPT). We initialize the atomic BEC in the six orbital states in  $\mathbb{S}$  and map

out the final quantum states following the holonomic quantum gates by TOFQST. The  $\chi$  matrices, which represent the quantum gate operations, are reconstructed by the QPT method [55,56]. The results are shown in Fig. 4. For completeness we also provide quantum process fidelities (QPFs) as defined by  $|\text{Tr}(\chi_{\text{exp}}\chi_{\text{th}}^\dagger)|/\sqrt{\text{Tr}(\chi_{\text{exp}}\chi_{\text{exp}}^\dagger)\text{Tr}(\chi_{\text{th}}\chi_{\text{th}}^\dagger)}$ , with  $\chi_{\text{exp}}$  and  $\chi_{\text{th}}$  being the  $\chi$  matrix reconstructed from experimental measurements and the theoretical expectation, respectively. The measured QPFs are 98.47(9)%, 98.35(11)%, 97.81(13)%, 98.53(8)%, and 98.63(15)%, for the  $X$ ,  $Y$ ,  $Z$ , Hadamard, and  $\pi/8$  gates, respectively, in the experiment.

*Discussion.* We have constructed an orbital qubit using atomic Bose-Einstein condensation in a one-dimensional optical lattice. The atom-orbital qubit is equipped with nonadiabatic holonomic quantum control, which shows noise resilience against laser intensity fluctuations due to geometrical protection (see Supplemental Material, Fig. S3 [26]). In order to further improve the gate fidelity in the experiment, we expect it is helpful to incorporate the inhomogeneity produced by the trap, which can be treated by integrating spin-echo-like pulse or optimal control protocols [44,57,58].

To achieve universal quantum computing with the orbital qubit setup, we still need to construct two-qubit gates, which can be implemented through an atom collision scheme (see Supplemental Material [26]). We expect the orbital quantum control techniques developed here can be generalized to full quantum control of all orbitals. For orbital transitions that respect parity symmetry, one may still take the lattice modulation protocol but using different resonant frequencies. To control orbital transitions violating parity symmetry would require lattice shaking techniques [59]. The orbital-lattice-based quantum computing would provide novel opportunities for programmable quantum simulations. For example, the demonstrated arbitrary coupling between  $s$  and  $d$  orbitals may be used to perform programmable quantum simulations of spin-orbital interaction analogs and the consequent topological physics [21].

We acknowledge helpful discussion with Yidun Wan. This work is supported by the National Natural Science Foundation of China (Grants No. 61727819, No. 11934002, No. 91736208, and No. 11774067), the National Program on Key Basic Research Project of China (Grants No. 2016YFA0301501 and No. 2017YFA0304204), and the Shanghai Municipal Science and Technology Major Project (Grant No. 2019SHZDZX01).

H.S., S.J., and Z.L. contributed equally to this work.

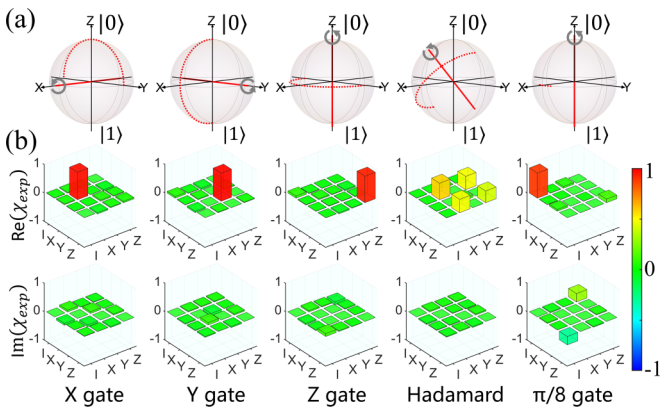


FIG. 4. Representations of the experimentally accomplished quantum processes. (a) The schematic illustration of the quantum processes. The red lines, gray arrows, and red dots represent the rotation axis, the direction, and the angle of the corresponding  $\text{SU}(2)$  rotation, respectively. (b) Process matrices of the implemented holonomic  $X$ ,  $Y$ ,  $Z$ , Hadamard, and  $\pi/8$  gates by QPT measurements.

- [1] R. J. Bartlett and M. Musiał, *Rev. Mod. Phys.* **79**, 291 (2007).
- [2] H. Hwang, Y. Iwasa, M. Kawasaki, B. Keimer, N. Nagaosa, and Y. Tokura, *Nat. Mater.* **11**, 103 (2012).
- [3] G. R. Stewart, *Rev. Mod. Phys.* **83**, 1589 (2011).
- [4] X. Li, J. Nan, and X. Pan, *Phys. Rev. Lett.* **125**, 263002 (2020).
- [5] Y. Liu, J. Xiao, J. Koo, and B. Yan, *Nat. Mater.* **20**, 638 (2021).
- [6] A. Aspuru-Guzik, A. Dutoi, P. Love, and M. Head-Gordon, *Science* **309**, 1704 (2005).
- [7] S. McArdle, S. Endo, A. Aspuru-Guzik, S. C. Benjamin, and X. Yuan, *Rev. Mod. Phys.* **92**, 015003 (2020).
- [8] A. Kandala, A. Mezzacapo, K. Temme, M. Takita, M. Brink, J. Chow, and J. Gambetta, *Nature (London)* **549**, 242 (2017).
- [9] G. A. Quantum, F. Arute, K. Arya, R. Babbush, D. Bacon, J. C. Bardin, R. Barends, S. Boixo, M. Broughton, B. B. Buckley *et al.*, *Science* **369**, 1084 (2020).
- [10] C. Hempel, C. Maier, J. Romero, J. McClean, T. Monz, H. Shen, P. Jurcevic, B. P. Lanyon, P. Love, R. Babbush, A. Aspuru-Guzik, R. Blatt, and C. F. Roos, *Phys. Rev. X* **8**, 031022 (2018).
- [11] Y. Nam, J.-S. Chen, N. Plesch, K. Wright, C. Delaney, D. Maslov, K. Brown, S. Allen, J. Amini, J. Apisdorf *et al.*, *npj Quantum Inf.* **6**, 1 (2020).
- [12] J. McClean, J. Romero, R. Babbush, and A. Aspuru-Guzik, *New J. Phys.* **18**, 023023 (2016).
- [13] X. Li and W. Liu, *Rep. Prog. Phys.* **79**, 116401 (2016).
- [14] A. Isacsson and S. M. Girvin, *Phys. Rev. A* **72**, 053604 (2005).
- [15] W. V. Liu and C. Wu, *Phys. Rev. A* **74**, 013607 (2006).
- [16] A. B. Kuklov, *Phys. Rev. Lett.* **97**, 110405 (2006).
- [17] G. Wirth, M. Ölschläger, and A. Hemmerich, *Nat. Phys.* **7**, 147 (2011).
- [18] P. Soltan-Panahi, D.-S. Lühmann, J. Struck, P. Windpassinger, and K. Sengstock, *Nat. Phys.* **8**, 71 (2012).
- [19] S. Jin, W. Zhang, X. Guo, X. Chen, X. Zhou, and X. Li, *Phys. Rev. Lett.* **126**, 035301 (2021).
- [20] K. Sun, W. Liu, A. Hemmerich, and S. Das Sarma, *Nat. Phys.* **8**, 67 (2012).
- [21] X. Li, E. Zhao, and W. Vincent Liu, *Nat. Commun.* **4**, 1523 (2013).
- [22] B. Liu, X. Li, B. Wu, and W. Liu, *Nat. Commun.* **5**, 5064 (2014).
- [23] M. Khamenechi, C. Qu, M. Mossman, C. Zhang, and P. Engels, *Nat. Commun.* **7**, 10867 (2016).
- [24] H. Lewis and W. Riesenfeld, *J. Math. Phys.* **10**, 1458 (1969).
- [25] U. Güngördü, Y. Wan, and M. Nakahara, *J. Phys. Soc. Jpn.* **83**, 034001 (2014).
- [26] See Supplemental Material at <http://link.aps.org/supplemental/10.1103/PhysRevA.104.L060601> for detailed simulation of the holonomic quantum control, and additional information on experimental protocols and data analysis.
- [27] X. Zhou, S. Jin, and J. Schmiedmayer, *New J. Phys.* **20**, 055005 (2018).
- [28] M. V. Berry, *Proc. R. Soc. Lond. A* **392**, 45 (1984).
- [29] S.-L. Zhu and Z. D. Wang, *Phys. Rev. Lett.* **89**, 097902 (2002).
- [30] M. Johansson, E. Sjöqvist, L. M. Andersson, M. Ericsson, B. Hessmo, K. Singh, and D. M. Tong, *Phys. Rev. A* **86**, 062322 (2012).
- [31] S. Berger, M. Pechal, A. A. Abdumalikov, C. Eichler, L. Steffen, A. Fedorov, A. Wallraff, and S. Filipp, *Phys. Rev. A* **87**, 060303(R) (2013).
- [32] G. Feng, G. Xu, and G. Long, *Phys. Rev. Lett.* **110**, 190501 (2013).
- [33] H. Li, Y. Liu, and G. Long, *Sci. China: Phys., Mech. Astron.* **60**, 080311 (2017).
- [34] C. Zu, W. Wang, L. He, W. Zhang, C. Dai, F. Wang, and L. Duan, *Nature (London)* **514**, 72 (2014).
- [35] S. Arroyo-Camejo, A. Lazariev, S. Hell, and G. Balasubramanian, *Nat. Commun.* **5**, 4870 (2014).
- [36] C. Yale, F. Heremans, B. Zhou, A. Auer, G. Burkard, and D. Awschalom, *Nat. Photonics* **10**, 184 (2016).
- [37] Y. Sekiguchi, N. Niikura, R. Kuroiwa, H. Kano, and H. Kosaka, *Nat. Photonics* **11**, 309 (2017).
- [38] F. Kleibler, A. Lazariev, and S. Arroyo-Camejo, *npj Quantum Inf.* **4**, 49 (2018).
- [39] Y.-Y. Huang, Y.-K. Wu, F. Wang, P.-Y. Hou, W.-B. Wang, W.-G. Zhang, W.-Q. Lian, Y.-Q. Liu, H.-Y. Wang, H.-Y. Zhang, L. He, X.-Y. Chang, Y. Xu, and L.-M. Duan, *Phys. Rev. Lett.* **122**, 010503 (2019).
- [40] P. Z. Zhao, X.-D. Cui, G. F. Xu, E. Sjöqvist, and D. M. Tong, *Phys. Rev. A* **96**, 052316 (2017).
- [41] K.-Y. Liao, X.-H. Liu, Z. Li, and Y.-X. Du, *Opt. Lett.* **44**, 4801 (2019).
- [42] B.-J. Liu, S.-L. Su, and M.-H. Yung, *Phys. Rev. Res.* **2**, 043130 (2020).
- [43] L.-M. Duan, J. I. Cirac, and P. Zoller, *Science* **292**, 1695 (2001).
- [44] K. Toyoda, K. Uchida, A. Noguchi, S. Haze, and S. Urabe, *Phys. Rev. A* **87**, 052307 (2013).
- [45] D. Leibfried, B. DeMarco, V. Meyer, D. Lucas, M. Barrett, J. Britton, W. M. Itano, B. Jelenković, C. Langer, T. Rosenband, and D. J. Wineland, *Nature (London)* **422**, 412 (2003).
- [46] M.-Z. Ai, S. Li, Z. Hou, R. He, Z.-H. Qian, Z.-Y. Xue, J.-M. Cui, Y.-F. Huang, C.-F. Li, and G.-C. Guo, *Phys. Rev. Appl.* **14**, 054062 (2020).
- [47] J. W. Zhang, L. L. Yan, J. C. Li, G. Y. Ding, J. T. Bu, L. Chen, S. L. Su, F. Zhou, and M. Feng, *Phys. Rev. Lett.* **127**, 030502 (2021).
- [48] A. A. Abdumalikov, Jr., J. M. Fink, K. Juliusson, M. Pechal, S. Berger, A. Wallraff, and S. Filipp, *Nature (London)* **496**, 482 (2013).
- [49] T. Yan, B.-J. Liu, K. Xu, C. Song, S. Liu, Z. Zhang, H. Deng, Z. Yan, H. Rong, K. Huang, M.-H. Yung, Y. Chen, and D. Yu, *Phys. Rev. Lett.* **122**, 080501 (2019).
- [50] Y. Xu, W. Cai, Y. Ma, X. Mu, L. Hu, T. Chen, H. Wang, Y. P. Song, Z.-Y. Xue, Z.-Q. Yin, and L. Sun, *Phys. Rev. Lett.* **121**, 110501 (2018).
- [51] Y. Xu, Z. Hua, T. Chen, X. Pan, X. Li, J. Han, W. Cai, Y. Ma, H. Wang, Y. P. Song, Z.-Y. Xue, and L. Sun, *Phys. Rev. Lett.* **124**, 230503 (2020).
- [52] Z. Zhang, P. Zhao, T. Wang, L. Xiang, Z. Jia, P. Duan, D. Tong, Y. Yin, and G. Guo, *New J. Phys.* **21**, 073024 (2019).
- [53] P. Zhao, Z. Dong, Z. Zhang, G. Guo, D. Tong, and Y. Yin, *Sci. China: Phys., Mech. Astron.* **64**, 250362 (2021).
- [54] P. O. Boykin, T. Mor, M. Pulver, V. Roychowdhury, and F. Vatan, On universal and fault-tolerant quantum computing: a novel basis and a new constructive proof of universality for Shor's basis, in *40th Annual Symposium on Foundations of Computer Science (Cat. No.99CB37039)* (IEEE, 1999), pp. 486–494.

- [55] M. Nielsen and I. Chuang, *Quantum Computation and Quantum Information*, 10th anniversary ed. (Cambridge University, Cambridge, England, 2010).
- [56] M. Howard, J. Twamley, C. Wittmann, T. Gaebel, F. Jelezko, and J. Wrachtrup, *New J. Phys.* **8**, 33 (2006).
- [57] B.-J. Liu, X.-K. Song, Z.-Y. Xue, X. Wang, and M.-H. Yung, *Phys. Rev. Lett.* **123**, 100501 (2019).
- [58] Y. Song, J. Lim, and J. Ahn, *Phys. Rev. Res.* **2**, 023045 (2020).
- [59] C. Parker, L.-C. Ha, and C. Chin, *Nat. Phys.* **9**, 769 (2013).